JOURNAL OF PROPULSION AND POWER
Vol. 26, No. 4, July–August 2010

Aerodynamic Heating of Reentry Body Equipped with Onboard-Surface Hall Magnetohydrodynamic Generator

Takayasu Fujino,* Tomoyuki Yoshino,† and Motoo Ishikawa‡
University of Tsukuba, Tsukuba 305-8573, Japan

DOI: 10.2514/1.45080

The generator performance and the aerodynamic heating of a reentry body equipped with an onboard-surface Hall-type magnetohydrodynamic power generator are examined under some different anode electrode configuration cases by means of two-dimensional numerical simulation. The reentry body with a nose radius of 1.35 m has a pair of electrodes on the wall surface. Flight altitude and velocity are set to 60 km and 5.6 km/s, respectively. The strength of an applied magnetic field is about 0.5 T. Numerical results demonstrate that the onboard-surface Hall-type magnetohydrodynamic power generator can effectively mitigate the wall heat flux at the stagnation point as well as extract the electrical power exceeding 1 MW when a ring-shaped anode electrode is placed on the wall surface away from the stagnation point. On the other hand, if a bowl-shaped anode electrode is placed to cover a wide wall surface including the stagnation point, an effective mitigation of the wall heat flux at the stagnation point by the magnetohydrodynamic interaction becomes impossible, although the electrical power exceeding 1 MW can be obtained. This is because a Hall electric field, strong enough to induce the strong magnetohydrodynamic interaction, cannot be obtained near the stagnation point, due to the electrically coupled circuit between the plasma and the bowl-shaped anode electrode.

Nomenclature

$\boldsymbol{B}$	=	magnetic field vector, T
B_r, B_z	=	components of magnetic flux density in the r and z directions, T
B_0	=	magnetic flux density at the stagnation point, T
D_s	=	effective diffusion coefficient of species s, m^2/s
$\hat{D}_s$	=	average vibrational energy of molecule s, which is created or destroyed at rate $\dot{\omega}_s$, J/kmol
E	=	total energy, J/kg
$\boldsymbol{E}$	=	electric field vector, V/m
E_r, E_z	=	components of electric field in the r and z directions, V/m
e	=	electronic charge, C
$\boldsymbol{e_r}$, $\boldsymbol{e_z}$	=	unit vectors in the r and z directions
e_{ve}	=	vibrational–electronic–electron energy, J/kg
$e_{v,s}$	=	vibrational energy of species s, J/kg
$e^*_{v,s}$	=	equilibrium vibrational energy of species s, J/kg
H	=	total enthalpy, J/kg
h_s	=	enthalpy of species s, J/kg
$h_{\mathrm{ve},s}$	=	vibrational–electronic–electron enthalpy of species s, J/kg
I	=	load current, A
I_s	=	first ionization energy of species s, J/kmol
$\boldsymbol{J}$	=	vector of electric current density, A/m^2
J_r, J_θ, J_z	=	components of electric current density in the r, θ, and z directions, A/m^2
k_b	=	Boltzmann's constant, J/K
$k_{b,i}$	=	backward reaction rate coefficient for reaction i, $m^3/(\mathrm{kmol}\cdot\mathrm{s})$ or $m^6/(\mathrm{kmol}^2\cdot\mathrm{s})$
$k_{f,i}$	=	forward reaction rate coefficient for reaction i, $m^3/(\mathrm{kmol}\cdot\mathrm{s})$
M_e	=	molecular weight of electron, kg/kmol
M_s	=	molecular weight of species s, kg/kmol
m	=	mobility of electron, $m^2/(\mathrm{V}\cdot\mathrm{s})$
m_e	=	mass of electron, kg
n_e	=	number density of electron, $1/m^3$
n_s	=	number density of species s, $1/m^3$
$\dot{n}_{e,s}$	=	molar rate of production of species s by electron impact ionization, $\mathrm{kmol}/(m^3\cdot\mathrm{s})$
P	=	electrical power extracted by magnetohydrodynamic power generator
P_∞	=	freestream pressure, Pa
p	=	static pressure, Pa
p_e	=	partial pressure of electron, Pa
p_s	=	partial pressure of species s, Pa
$\bar{R}$	=	universal gas constant, $\mathrm{J}/(\mathrm{kmol}\cdot\mathrm{K})$
Q	=	total aerodynamic heating, W
q_{stag}	=	wall heat flux at stagnation point, W/m^2
q_{wall}	=	wall heat flux, W/m^2
R_b	=	nose-radius of body, m
R_{ext}	=	external load resistance, Ω
$R_{f,i}$, $R_{b,i}$	=	forward and backward reaction rates for reaction i, $\mathrm{kmol}/(m^3\cdot\mathrm{s})$
r, θ, z	=	cylindrical coordinates
T_{tr}	=	translational–rotational temperature, K
T_{ve}	=	vibrational–electronic–electron temperature, K
T_W	=	wall temperature, K
T_∞	=	freestream temperature, K
t	=	time, s
U_∞	=	freestream velocity, m/s
u_r, u_θ, u_z	=	velocity components in the r, θ, and z directions, m/s
V_L	=	load voltage, V
y_s	=	mole fraction of species s
$\alpha_{s,i}$, $\beta_{s,i}$	=	forward and backward stoichiometric coefficients of species s in reaction i
β	=	electron Hall parameter
ϵ_0	=	permittivity of vacuum, F/m
η_{tr}	=	mixture translational–rotational thermal conductivity, $W/(m\cdot K)$
η_{ve}	=	mixture vibrational–electron thermal conductivity, $W/(m\cdot K)$

Presented as Paper 2008-4225 at the 39th Plasmadynamics and Lasers Conference, Seattle, WA, 23–26 June 2008; received 22 April 2009; revision received 18 February 2010; accepted for publication 25 March 2010.

*Assistant Professor, Graduate School of Systems and Information Engineering. Member AIAA.

†Graduate Student, Graduate School of Systems and Information Engineering. Student Member AIAA.

‡Professor, Graduate School of Systems and Information Engineering. Senior Member AIAA.

μ = mixture viscosity, kg/(m · s)
$\nu_{e,s}$ = effective energy exchange collision frequency of electron with species s, 1/s
$\nu^m_{e,s}$ = effective momentum transfer collision frequency of electron with species s, 1/s
ξ, η = generalized curvilinear coordinates
ρ = total mass density, kg/m^3
ρ_e = mass density of electron, kg/m^3
ρ_s = mass density of species s, kg/m^3
σ = electrical conductivity, S/m
$\sigma^m_{e,s}$ = effective collision cross section of electrons with neutral species s, m^2
$\tau_{i,j}$ = viscous shear stress
τ_s = translational–vibrational energy relaxation time of species s, s
ϕ = electric potential, V
ϕ_{anode} = electric potential on anode electrode, V
ϕ_{cathode} = electric potential on cathode electrode, V
$\dot{\omega}_s$ = mass production rate of species s, kg/(m^3 · s)
$\dot{\omega}_{\text{ve}}$ = production rate of vibrational–electronic–electron energy, J/(m^3 · s)

I. Introduction

A NUMBER of feasibility studies on applications of magnetohydrodynamic (MHD) technology to the aerospace engineering field have been conducted both numerically and experimentally by many researchers in the United States, Russia, Japan, and many other nations.

As one of the MHD applications, an active thermal protection technique in reentry flights using the MHD technology, which is called the MHD thermal protection or the MHD heat shield, was proposed in 1950s (for example, see [1–3]). The outline of the concept of the MHD thermal protection is as follows: when the magnetic field is applied to the weakly ionized plasma flow in the shock layer around a reentry vehicle, the electric current is induced in the shock layer. The interaction between the electric current and the magnetic field produces the Lorentz force, which decelerates the plasma flow in the shock layer and increases the shock standoff distance. Consequently, the aerodynamic heating can be reduced.

As one of other MHD applications in Earth-reentry or planetary-entry flights, the concept of onboard-surface MHD power generators during Earth-reentry flights was proposed by Bityurin et al. [4]. They also suggested, as an example of the usages of extracted electrical power, that the extracted electrical power could be used by a flight control system to optimize reentry trajectories and particular maneuvers. Based on this proposal, Macheret et al. [5] theoretically explored the possibility of an onboard-surface MHD power generator classified as Faraday-type MHD power generator during Earth-reentry flights, and they concluded that the substantial amounts of electrical power from several hundred kilowatts to a few megawatts per square meter from the surface at altitudes of 45–60 km and flight velocities of 6–7 km/s can be extracted with a modest amount (1%) of alkali seed and applied magnetic field of $0.1 - 0.2$ T. Their research group has continued feasibility studies on the onboard-surface Faraday-type MHD power generator using a more sophisticated three-dimensional computational code, including finite rate ionization model [6,7].

In recent years the authors have carried out the feasibility studies of the MHD thermal protection by means of numerical simulation (for example, see [8–11]). The numerical studies have been conducted mainly under the OREX (Orbital Reentry Experiments, in Japan, 1994) reentry experimental flight condition at an altitude of about 60 km (flight velocity: 5.6 km/s), where it was observed that the aerodynamic heating peaked [12]. The numerical results showed that an applied dipole magnetic field of about 0.5 T reduced the wall heat flux at the stagnation point by about 80% compared to the value in the case of no magnetic field [9]. It was also found that the Hall effect dominated the electrodynamics in the shock layer. Figure 1, which was obtained in our previous study on the MHD thermal protection [9], depicts the distribution of electric potential ahead of the

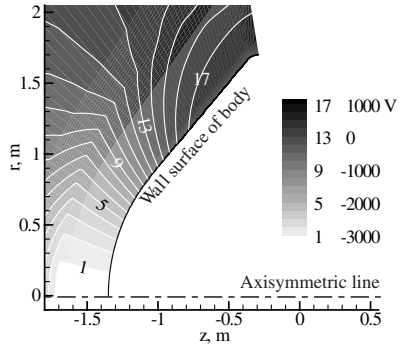

Fig. 1 Distribution of electric potential on the *r-z* plane induced by the Hall effect shown in authors' previous numerical study [9]. Note that the distribution is obtained in the case without electrodes for extracting electrical power.

axisymmetric *r-z* two-dimensional blunt-body OREX with a nose radius of 1.35 m when the dipole magnetic field of about 0.5 T is applied at the altitude of about 60 km. As shown in Fig. 1, the Hall effect induces the electric potential elevation of about 4 kV from the stagnation point to the shoulder of the body. Based on this result, the authors have proposed an onboard-surface Hall-type MHD power generator for converting a part of the kinetic energy of reentry flow into the electrical energy. We also have numerically conducted the conceptual demonstration of the onboard-surface Hall-type MHD power generator [13]. Figure 2 illustrates the configuration of the onboard-surface Hall-type MHD power generator supposed in [13], in which two electrodes: a bowl-shaped anode electrode and a ring-shaped cathode electrode are mounted on the wall surface of the nose of a reentry space vehicle. The numerical results in [13] showed that the electrical power of a few megawatts could be obtained by the onboard-surface Hall-type MHD generator with the dipole magnetic field of about 0.5 T under the OREX reentry flight condition at the altitude of about 60 km.

The numerical results also showed that the Hall electric field in the flowfield ahead of the bowl-shaped anode electrode covering the stagnation point was almost zero. As a result, the strong MHD interaction could not be obtained around the stagnation point. Consequently, the wall heat flux around the stagnation point could not be effectively reduced by the applied magnetic field unlike the case without an electrode.

The authors expect that the strong Hall electric field will be generated in the flowfield around the stagnation point by mounting a ring-shaped anode electrode on the wall surface away from the stagnation point. As a result, the effective mitigation of the wall heat flux around the stagnation point as well as the extraction of electrical power of a few megawatts will become possible.

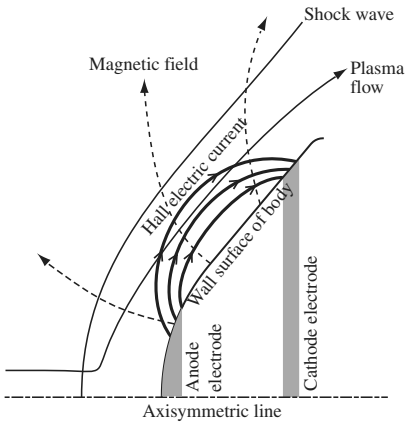

Fig. 2 Onboard-surface Hall-type MHD power generator supposed in authors' previous numerical study [13].

The present numerical study therefore examines the influences of the anode electrode configuration (shape and position) on the aerodynamic heating as well as the generator performance of the reentry body equipped with the onboard-surface Hall-type MHD power generator.

II. Numerical Methods and Numerical Conditions

A. Configuration of Anode and Cathode Electrodes of Onboard-Surface Hall-Type MHD Power Generator

A reentry body equipped with the onboard-surface Hall-type MHD power generator has anode and cathode electrodes on the wall surface of its forebody. Figure 3 illustrates the forebody shape of the reentry body and the electrode configuration cases supposed in the present numerical study. The forebody shape, which is identical to that of the blunt-body OREX used in the reentry experiments in Japan (1994) [12], is composed of a spherical nose with a radius of 1.35 m, a cone, and a circular shoulder. The position and the shape of the cathode electrode are the same for any electrode configuration case, but the position or the shape of anode electrode is different for each case. In case 1, a bowl-shaped anode electrode covers the wide area of the wall surface including the stagnation point; our previous numerical study in [13] was conducted for case 1. In case 2, case 3, and case 4, a ring-shaped anode electrode is mounted on the wall surface away from the stagnation point. The distance between the anode and the cathode electrodes in case 2 is almost the same as that in case 1. Of case 2, case 3, and case 4, case 2 has the longest distance between the electrodes; case 4 has the shortest distance between the electrodes, as can be seen from Fig. 3. The present study assumes that the load resistance is connected between the electrodes, and also that the load voltage is adjusted by varying the value of the load resistance.

B. Flight Condition and Distribution of Applied Magnetic Field

The present numerical simulations are carried out under the flight condition at the altitude of 59.6 km in the OREX experiments as follows: the freestream pressure P_∞ is 23.6 Pa, the freestream temperature T_∞ is 248.1 K, and the freestream velocity U_∞ is 5562 m/s [12]. Under the flight condition, the aerodynamic heating had a peak value in the OREX experiments. It is well known that the electrical conductivity and the Hall parameter, which directly affect the generator performance, strongly depend on flight conditions. We are therefore planning to examine the generator performance for a wide range of flight conditions in the near future.

Figure 4 shows the distribution of an externally applied magnetic field, which is expressed by

$$\boldsymbol{B}(r,z) = -\frac{B_0 R_b^3}{2(z^2+r^2)^{3/2}}\left[\left(\frac{2z^2}{z^2+r^2}-\frac{r^2}{z^2+r^2}\right)\boldsymbol{e}_z + \frac{3zr}{z^2+r^2}\boldsymbol{e}_r\right] \quad (1)$$

In the present study, the value of the parameter B_0 in Eq. (1) is fixed to 0.5 T. The externally applied magnetic field is assumed to be produced by a punctiform dipole magnet placed at the point of $r = 0$ m and $z = 0$ m inside the blunt body. The generator performance of the onboard-surface Hall-type MHD power generator using a more realistic magnet such as an air-core superconducting magnet will be examined in our future study.

C. Basic Equations for Gas Dynamics and Electrodynamics

The present study addresses the flowfield and the electromagnetic field as the axisymmetric two-dimensional field (r-z). The basic equations for the gas dynamics are the mass conservation equations of chemical species, the momentum conservation equations, the total energy conservation equation, and the vibrational–electronic–electron energy conservation equation. We consider the following 11 chemical species: N, O, N_2, O_2, NO, N^+, O^+, N_2^+, O_2^+, NO^+, and e^-. Kang et al.'s model [14] is used as a finite rate chemical kinetics model. Park's two-temperature model [15] is employed in order to take account of the thermal nonequilibrium state. The basic equations for the gas dynamics are written as follows.

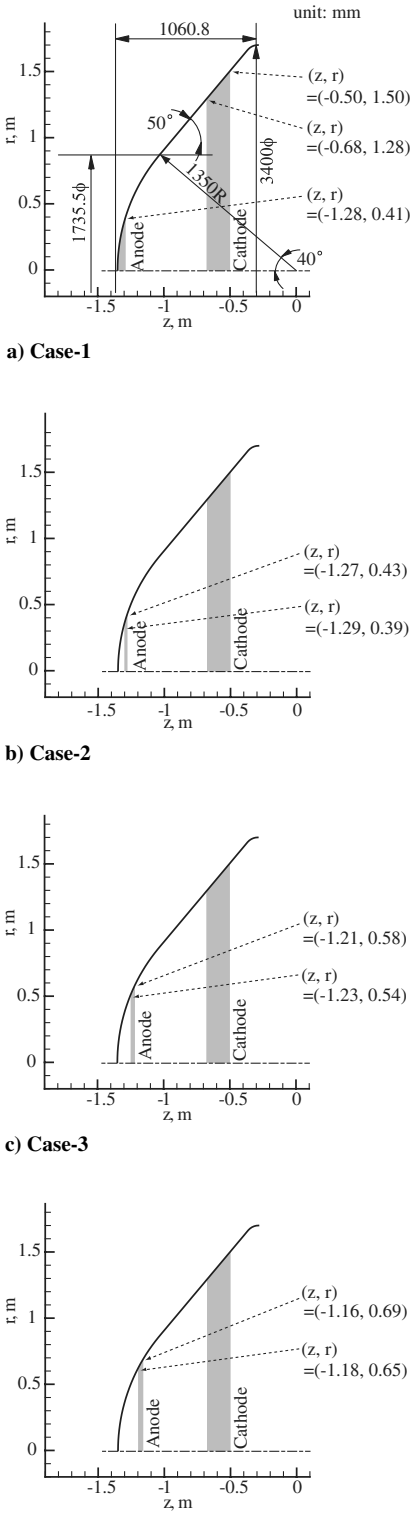

Fig. 3 Forebody shape of reentry body and different electrode configuration cases.

Mass conservation equations of chemical species (s = N, O, N_2, O_2, NO, N^+, O^+, N_2^+, O_2^+, NO^+, and e^-):

$$\frac{\partial \rho_s}{\partial t} + \frac{\partial}{\partial r}(\rho_s u_r) + \frac{\partial}{\partial z}(\rho_s u_z) = \dot{\omega}_s + \frac{\partial}{\partial r}\left(\rho D_s \frac{\partial y_s}{\partial r}\right) + \frac{\partial}{\partial z}\left(\rho D_s \frac{\partial y_s}{\partial z}\right) - \frac{1}{r}\left(\rho_s u_r - \rho D_s \frac{\partial y_s}{\partial r}\right) \quad (2)$$

where the total mass density ρ is given by

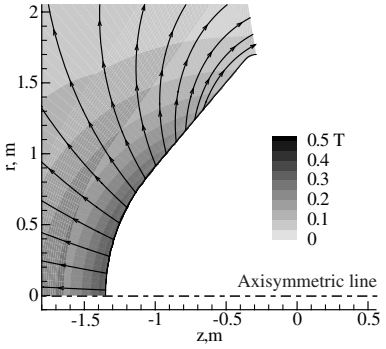

Fig. 4 Distribution of applied magnetic field.

$$\rho = \sum_s \rho_s \tag{3}$$

The first term $\dot{\omega}_s$ on the right-hand side of Eq. (2) is the source term for the mass production rate of species s and is expressed as

$$\dot{\omega}_s = M_s \sum_{i=1}^{32} (\beta_{s,i} - \alpha_{s,i})(R_{f,i} - R_{b,i}) \tag{4}$$

The forward and backward reaction rates, $R_{f,i}$ and $R_{b,i}$ are, respectively, defined by

$$R_{f,i} = k_{f,i} \prod_{s=1}^{11} (\rho_s / M_s)^{\alpha_{s,i}}, \qquad R_{b,i} = k_{b,i} \prod_{s=1}^{11} (\rho_s / M_s)^{\beta_{s,i}} \tag{5}$$

where the forward reaction rate coefficients $k_{f,i}$ and the backward reaction rate coefficients $k_{b,i}$ are tabulated in [14,16].

Momentum conservation equations:

$$\frac{\partial \rho u_r}{\partial t} + \frac{\partial}{\partial r}(\rho u_r^2 + p) + \frac{\partial}{\partial z}(\rho u_r u_z) = \frac{\partial \tau_{rr}}{\partial r} + \frac{\partial \tau_{rz}}{\partial z} + J_\theta B_z - \frac{1}{r}(\rho(u_r^2 - u_\theta^2) - \tau_{rr} + \tau_{\theta\theta}) \tag{6}$$

$$\frac{\partial \rho u_\theta}{\partial t} + \frac{\partial}{\partial r}(\rho u_\theta u_r) + \frac{\partial}{\partial z}(\rho u_\theta u_z) = \frac{\partial \tau_{r\theta}}{\partial r} + \frac{\partial \tau_{z\theta}}{\partial z} + J_z B_r - J_r B_z - \frac{2}{r}(\rho u_r u_\theta - \tau_{r\theta}) \tag{7}$$

$$\frac{\partial \rho u_z}{\partial t} + \frac{\partial}{\partial r}(\rho u_z u_r) + \frac{\partial}{\partial z}(\rho u_z^2 + p) = \frac{\partial \tau_{rz}}{\partial r} + \frac{\partial \tau_{zz}}{\partial z} - J_\theta B_r - \frac{1}{r}(\rho u_r u_z - \tau_{rz}) \tag{8}$$

where the static pressure p and the viscous stress terms $\tau_{i,j}$ are defined by

$$p = \sum_s p_s = \sum_{s=1-10} \rho_s \frac{\bar{R}}{M_s} T_{\mathrm{tr}} + \rho_e \frac{\bar{R}}{M_e} T_{\mathrm{ve}} \tag{9}$$

$$\tau_{rr} = \frac{2}{3}\mu\left(2\frac{\partial u_r}{\partial r} - \frac{\partial u_z}{\partial z} - \frac{u_r}{r}\right), \quad \tau_{\theta\theta} = \frac{2}{3}\mu\left(2\frac{u_r}{r} - \frac{\partial u_r}{\partial r} - \frac{\partial u_z}{\partial z}\right)$$
$$\tau_{zz} = \frac{2}{3}\mu\left(2\frac{\partial u_z}{\partial z} - \frac{\partial u_r}{\partial r} - \frac{u_r}{r}\right), \quad \tau_{r\theta} = \tau_{\theta r} = \mu\left(\frac{\partial u_\theta}{\partial r} - \frac{u_\theta}{r}\right)$$
$$\tau_{rz} = \tau_{zr} = \mu\left(\frac{\partial u_r}{\partial z} + \frac{\partial u_z}{\partial r}\right), \quad \tau_{\theta z} = \tau_{z\theta} = \mu\frac{\partial u_\theta}{\partial z} \tag{10}$$

Total energy conservation equation:

$$\frac{\partial \rho E}{\partial t} + \frac{\partial}{\partial r}(\rho H u_r) + \frac{\partial}{\partial z}(\rho H u_z) = \frac{\partial}{\partial r}\left(\eta_{\mathrm{tr}}\frac{\partial T_{\mathrm{tr}}}{\partial r} + \eta_{\mathrm{ve}}\frac{\partial T_{\mathrm{ve}}}{\partial r}\right) + \frac{\partial}{\partial z}\left(\eta_{\mathrm{tr}}\frac{\partial T_{\mathrm{tr}}}{\partial z} + \eta_{\mathrm{ve}}\frac{\partial T_{\mathrm{ve}}}{\partial z}\right) + \frac{\partial}{\partial r}\left(\rho\sum_s h_s D_s \frac{\partial y_s}{\partial r}\right) + \frac{\partial}{\partial z}\left(\rho\sum_s h_s D_s \frac{\partial y_s}{\partial z}\right) + \frac{\partial}{\partial r}(\tau_{rr}u_r + \tau_{\theta r}u_\theta + \tau_{zr}u_z) + \frac{\partial}{\partial z}(\tau_{rz}u_r + \tau_{\theta z}u_\theta + \tau_{zz}u_z) + J_r E_r + J_z E_z - \frac{\rho H u_r}{r} + \frac{\rho}{r}\sum_s h_s D_s \frac{\partial y_s}{\partial r} + \frac{1}{r}\left(\eta_{\mathrm{tr}}\frac{\partial T_{\mathrm{tr}}}{\partial r} + \eta_{\mathrm{ve}}\frac{\partial T_{\mathrm{ve}}}{\partial r}\right) + \frac{1}{r}(\tau_{rr}u_r + \tau_{\theta r}u_\theta + \tau_{zr}u_z) \tag{11}$$

where the total enthalpy H is defined as

$$H = E + \frac{p}{\rho} \tag{12}$$

Vibrational–electronic–electron energy conservation equation:

$$\frac{\partial \rho e_{\mathrm{ve}}}{\partial t} + \frac{\partial}{\partial r}(\rho e_{\mathrm{ve}} u_r) + \frac{\partial}{\partial z}(\rho e_{\mathrm{ve}} u_z) = \dot{\omega}_{\mathrm{ve}} + \frac{\partial}{\partial r}\left(\eta_{\mathrm{ve}}\frac{\partial T_{\mathrm{ve}}}{\partial r}\right) + \frac{\partial}{\partial z}\left(\eta_{\mathrm{ve}}\frac{\partial T_{\mathrm{ve}}}{\partial z}\right) + \frac{\partial}{\partial r}\left(\rho\sum_s h_{\mathrm{ve},s} D_s \frac{\partial y_s}{\partial r}\right) + \frac{\partial}{\partial z}\left(\rho\sum_s h_{\mathrm{ve},s} D_s \frac{\partial y_s}{\partial z}\right) + \frac{J_r^2 + J_\theta^2 + J_z^2}{\sigma} - \frac{1}{r}\left(\rho e_{\mathrm{ve}} u_r - \rho\sum_s h_{\mathrm{ve},s} D_s \frac{\partial y_s}{\partial r} - \eta_{\mathrm{ve}}\frac{\partial T_{\mathrm{ve}}}{\partial r}\right) \tag{13}$$

where $\dot{\omega}_{\mathrm{ve}}$ is the source term for the production rate of vibrational–electronic–electron energy and is expressed as

$$\dot{\omega}_{\mathrm{ve}} = \sum_{s=\mathrm{mol}} \rho_s \frac{e_{v,s}^* - e_{v,s}}{\langle \tau_s \rangle} + 2\rho_e \frac{3}{2}\bar{R}(T_{\mathrm{tr}} - T_{\mathrm{ve}}) \sum_{s\neq e} \frac{\nu_{e,s}}{M_s} - \sum_{s=\mathrm{ion}} \dot{n}_{e,s} I_s + \sum_{s=\mathrm{mol}} \dot{\omega}_s \hat{D}_s - p_e\left(\frac{\partial u_r}{\partial r} + \frac{\partial u_z}{\partial z} + \frac{u_r}{r}\right) \tag{14}$$

where the relaxation time τ_s of each species for a translational–vibrational energy relaxation is calculated from the sum of the relaxation time formula proposed by Millikan and White [17] and the correction term suggested by Park [15]. The effective energy exchange frequency ν_{es} of electrons with other species is estimated by following [16]. The average vibrational energy $\hat{D}_s$, which is created or destroyed at the rate $\dot{\omega}_s$, is computed by using the nonpreferential model [16].

The transport coefficients such as the effective diffusion coefficient D_s of each species, the mixture viscosity μ, the mixture translational–rotational thermal conductivity η_{tr}, and the mixture vibrational–electron thermal conductivity η_{ve} are estimated by an extension model of Yos' formulas to the multitemperature gas mixture (see [16]).

The basic equations for the electrodynamics are the continuity equation of steady electric currents and the generalized Ohm's law.

Continuity equation of steady electric currents:

$$\nabla \cdot \boldsymbol{J} = 0 \tag{15}$$

Generalized Ohm's law:

$$\begin{pmatrix} J_r \\ J_\theta \\ J_z \end{pmatrix} = \frac{\sigma}{1+\beta^2} \begin{pmatrix} 1+m^2B_r^2 & -mB_z & m^2B_rB_z \\ mB_z & 1 & -mB_r \\ m^2B_rB_z & mB_r & 1+m^2B_z^2 \end{pmatrix} \begin{pmatrix} E_r + u_\theta B_z + \frac{1}{en_e}\frac{\partial p_e}{\partial r} \\ u_zB_r - u_rB_z \\ E_z - u_\theta B_r + \frac{1}{en_e}\frac{\partial p_e}{\partial z} \end{pmatrix}$$

$$\boldsymbol{E} = -\nabla\phi \tag{16}$$

The electrical conductivity σ, the Hall parameter β, and the mobility of electron m are, respectively, expressed as

$$\sigma = \frac{n_e e^2}{m_e \sum_{s\neq e} \nu_{e,s}^m}, \qquad \beta = \frac{e|\boldsymbol{B}|}{m_e \sum_{s\neq e} \nu_{e,s}^m}, \qquad m = \frac{\beta}{|\boldsymbol{B}|} \tag{17}$$

The effective momentum transfer collision frequency $\nu_{e,s}^m$ of electrons with the other chemical species [18,19] s is written as

$$\nu_{e,s}^m = \begin{cases} 6\pi\left(\frac{e^2}{12\pi\epsilon_0 k_b T_{\rm ve}}\right)^2 \ell_n\left[12\pi\left(\frac{\epsilon_0 k_b}{e^2}\right)^{3/2}\sqrt{\frac{T_{\rm ve}^3}{n_e}}\right] n_s \sqrt{\frac{8k_bT_{\rm ve}}{\pi m_e}} & \text{if } s \text{ is ion species} \\ \frac{4}{3}\sigma_{e,s}^m n_s \sqrt{\frac{8k_bT_{\rm ve}}{\pi m_e}} & \text{otherwise} \end{cases} \tag{18}$$

where the effective collision cross section of electrons with the other neutral chemical species s $\sigma_{e,s}$ is computed using the curve fit presented in [16]; the curve fit was generated from the effective collision cross-sectional data in [20]. For the flight condition considered, the translational–rotational temperature $T_{\rm tr}$ and the vibrational–electronic–electron temperature $T_{\rm ve}$ in the vicinity of shock front, about 12,000 and 8000 K, respectively, are in a nonequilibrium state. However, just upstream of shock layer, the translational–rotational temperature $T_{\rm tr}$ and the vibrational–electronic–electron temperature $T_{\rm ve}$ are in an equilibrium state with a temperature of approximately 7000–8000 K [10]. The overall effective transfer collision frequency of electrons

$$\sum_{s\neq e} \nu_{e,s}^m$$

in the shock layer is on the order of 10^9 1/s. The collision frequency of electrons with N_2, which is on the order of 10^9 1/s, contributes most to the overall effective transfer collision frequency of electrons, followed by the collision frequency of electrons with NO^+, which is on the order of 10^8 1/s.

In the present study, the ion-slip term in the generalized Ohm's law is neglected for simplicity. As shown in our previous numerical studies [9,10,13], the electron Hall parameter in the shock layer is about 10–15 under the present flight condition. From the value of the electron Hall parameter, the ion Hall parameter is estimated at the order of 0.1, and so the product of electron and ion Hall parameters is estimated at the order of 1 [21]. The ratio of the ion-slip term to the Hall term in the generalized Ohm's law is estimated at the order of 0.1. We therefore think that the ion-slip phenomenon does not make considerable differences from the numerical results obtained in the present study, in which the ion-slip effect is neglected.

D. Numerical Procedure

A computational region and a computational grid (normal grid) are illustrated in Fig. 5. The number of grid points is 65 in the ξ direction along the wall surface and 250 in the outward η direction. Since the prediction of the wall heat flux is extremely sensitive to the mesh size near the wall surface, the dependence of the wall heat flux on the mesh size near the wall surface was checked in advance. Based on the check, we set the minimum mesh size near the wall surface to about 2 μm. Furthermore, the authors checked the dependence of the generator performance on computational grids under the maximum electrical power condition in case 1 ($V_L = 2931$ V). For the check, the number of the grid point in the η direction in the shock layer was changed. The computed electrical power had a slightly decreasing tendency with increase of the grid point in the η direction. The difference of electrical power between a coarse grid ($\xi 65 \times \eta 170$) and the normal grid ($\xi 65 \times \eta 250$) was about 2.3% of the electrical power in the normal grid. The difference between a fine grid ($\xi 65 \times \eta 350$) and the normal grid ($\xi 65 \times \eta 250$) was only about 0.5% of the electrical power in the normal grid. The difference of electrical power between the fine grid and the normal grid has no influence on the discussion in the present paper. The normal grid illustrated in

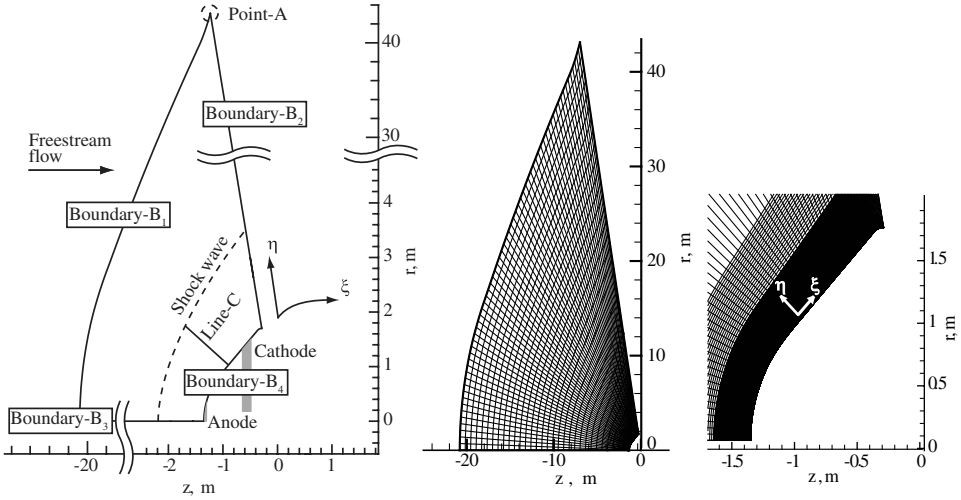

Fig. 5 Computational region and computational grid.

Fig. 5 is therefore employed for all numerical simulations shown in the present paper.

The conservation equations of the gas dynamics are expressed in terms of a generalized curvilinear coordinate system and discretized using a structured finite volume approach. The numerical flux for the convective term is constructed by the advection upstream splitting method (AUSM)-DV [22]. The MUSCL approach [23] with the minmod limiter function is used to achieve higher-order evaluation of the primitive variables in AUSM-DV scheme. As for the diffusion, viscous, and thermal conduction terms, the second-order central-differencing scheme is used. The time integration is performed by the lower-upper symmetric Gauss–Seidel (LU-SGS) implicit scheme [24]. In the present study, the diagonal point implicit method proposed by Eberhardt and Imlay [25], which can eliminate the stiffness problem associated with finite chemical reaction, is incorporated into the LU-SGS scheme. The boundary conditions for the gas dynamics are specified as follows. For inflow (the boundary line B_1 in Fig. 5), the freestream conditions are given as

$$\frac{\rho_{N_2}}{\rho} = 0.79, \qquad \frac{\rho_{O_2}}{\rho} = 0.21, \qquad u_z = U_\infty, \qquad u_r = u_\theta = 0$$

$$p = P_\infty, \qquad T_{tr} = T_{ve} = T_\infty$$

For outflow (the boundary line B_2 in Fig. 5), the gradients of all primitive variables (ρ_s, u_z, u_r, u_θ, T_{tr}, and T_{ve}) in the ξ direction are set to zero. For the symmetric line (the boundary line B_3 in Fig. 5), u_r and u_θ are set to zero, and the normal gradient is set to zero for the other primitive variables (ρ_s, u_z, T_{tr}, and T_{ve}). For the wall surface (the boundary line B_4 in Fig. 5), the no-slip condition, the fixed wall temperature condition, and the noncatalytic wall condition are used, and the translational–rotational temperature T_{tr} and the vibrational–electron temperature T_{ve} on the wall surface are assumed to be equilibrium with the wall temperature T_W. The wall temperature T_W is set to 1519 K; this value corresponds to the wall temperature at the stagnation point estimated at the altitude of about 60 km in the OREX experiments.

We derive the second-order partial differential equation on the electric potential ϕ from Eqs. (15) and (16):

$$\begin{aligned}
&\frac{1}{r}\frac{\partial}{\partial r}\left[r\frac{\sigma}{1+\beta^2}\left\{(1+m^2B_r^2)\left(-\frac{\partial\phi}{\partial r}+u_\theta B_z+\frac{1}{en_e}\frac{\partial p_e}{\partial r}\right)\right.\right.\\
&\left.\left.-mB_z(u_zB_r-u_rB_z)+m^2B_rB_z\left(-\frac{\partial\phi}{\partial z}-u_\theta B_r+\frac{1}{en_e}\frac{\partial p_e}{\partial z}\right)\right\}\right]\\
&+\frac{\partial}{\partial z}\left[\frac{\sigma}{1+\beta^2}\left\{m^2B_rB_z\left(-\frac{\partial\phi}{\partial r}+u_\theta B_z+\frac{1}{en_e}\frac{\partial p_e}{\partial r}\right)\right.\right.\\
&+mB_r(u_zB_r-u_rB_z)+(1+m^2B_z^2)\left(-\frac{\partial\phi}{\partial z}-u_\theta B_r\right.\\
&\left.\left.\left.+\frac{1}{en_e}\frac{\partial p_e}{\partial z}\right)\right\}\right]=0
\end{aligned} \tag{19}$$

The equation is discretized by the Galerkin finite element method (FEM) with the first-order triangular shape functions. A set of the obtained linear algebraic equations with a symmetric band matrix is solved with Gaussian elimination method.

The boundary conditions for the case with extracted electrical power are as follows.

1) For inflow (the boundary line B_1 in Fig. 5), outflow (the boundary line B_2 in Fig. 5), the symmetric line (the boundary line B_3 in Fig. 5), and the wall surface (the boundary line B_4 in Fig. 5), the normal component of electric current density on the boundary lines is set to 0 A/m^2.

2) For the anode electrode, the electric potential ϕ_{anode} on the anode electrode is set to 0 V.

3) For the cathode electrode, the electric potential $\phi_{cathode}$ on the cathode electrode, that is, the load voltage V_L is given as

$$\phi_{cathode} = V_L = R_{ext} \cdot I$$

where the load current I is obtained by computing the surface integral of the electric current density perpendicular to the line C in Fig. 5.

The present study also includes the numerical simulation for the case without electrodes, that is, the case without electrical power extraction. The boundary conditions for the case without electrodes are as follows: the normal component of electric current density is set to 0 A/m^2 on all boundary lines in Fig. 5, whereas the electric potential ϕ at the point A in Fig. 5 is set to 0 V for establishing a reference value of electric potential.

From the obtained electric potential distribution and the generalized Ohm's law, we evaluate the electric field and the electric current density in the source term for the MHD interaction in the conservation equations of gas dynamics. The conservation equations of gas dynamics and the electric potential equation are solved iteratively until the steady state solutions are obtained. In the iterative computation process, the gas dynamics is coupled with the electrodynamics through the source term for the MHD interaction.

Power-generation experiments using a test body with a Hall-type MHD power-generation system as proposed here have not yet been conducted either in a ground hypersonic tunnel environment or in a real reentry-fight environment. As a result, the solver of gas dynamics, including thermochemical reaction models, and the solver of electrodynamics were validated separately. As shown in [26], we compared the shock location of both numerical results and experimental data in Lobb's experiments [27] to validate the reliability of the numerical solutions for the gas-dynamics part, including thermochemical reactions. As a result, good agreement between numerical results and experimental data was obtained. The electrodynamics part in the developed computational code has been widely used for many years in our numerical studies (for example, [28,29]) on MHD power generators such as a large-scale Faraday-type MHD generator Sakhalin with the electrical power of 510 MW [28] and a shock-tube-driven Hall-type MHD power generator in the Tokyo Institute of Technology with high generator efficiency [29]. These numerical studies have clearly shown that the reliability of the numerical solutions for the electrodynamics part is very high.

III. Results and Discussion

Figure 6 depicts the relationship between electrical power and load voltage for each electrode configuration case. Figure 7 illustrates the current-voltage characteristics for each electrode configuration case. The electrical power of more than 1 MW is extracted for any electrode configuration though the maximum electrical power strongly depends on the electrode configurations, as shown in Fig. 6. As can be also found from Figs. 3 and 6, the maximum electrical power decreases as the distance between the anode and the cathode electrodes becomes shorter. This is mainly because the power extraction volume reduces with decreasing the distance between the electrodes. We can also find from Fig. 6 that the load voltage with the maximum electrical power, which is called optimum load voltage here, decreases with a decrease in distance between the electrodes. This is because the decrease in distance between the electrodes leads to a decrease in open voltage between the electrodes, as can be predicted from Fig. 7. We have estimated the open voltage for each

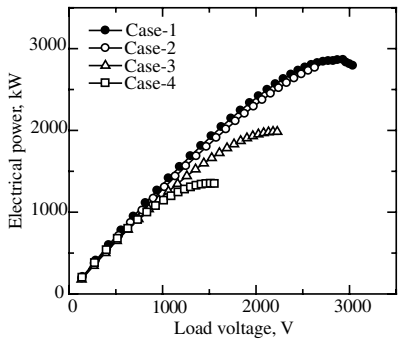

Fig. 6 Relationship between electrical power and load voltage for each electrode configuration case.

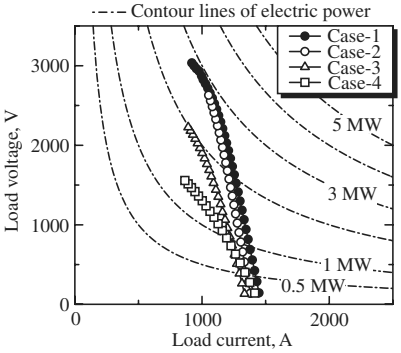

Fig. 7 Characteristics of load current and load voltage for each electrode configuration case.

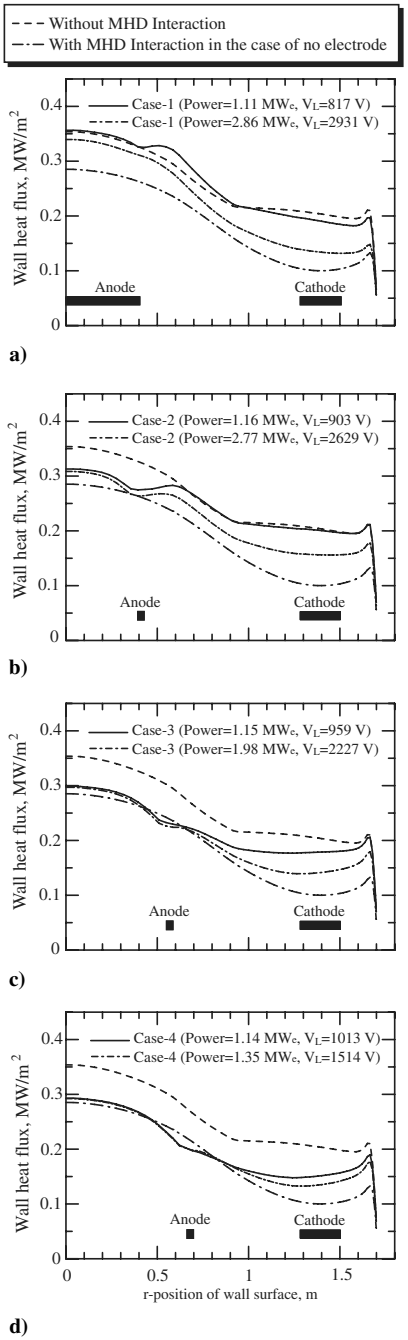

Fig. 8 Wall heat flux for each electrode configuration case.

electrode configuration case from the distribution of Hall electric potential for the no-electrode case illustrated in Fig. 1. The open voltage estimated is about 3.6 kV for case 1 and case 2, 3.0 kV for case 3, and 2.5 kV for case 4, respectively.

Figure 6 also shows there is little difference in the electrical power between case 1 and case 2 under same load voltage condition. Furthermore, case 1 and case 2 have almost the same current-voltage characteristics, as shown in Fig. 7. The distance between the anode and the cathode electrodes in case 1 is almost the same as that in case 2; however, case 1 differs considerably from case 2 in the surface area of anode electrode, as illustrated in Fig. 3. The comparison between case 1 and case 2 in Figs. 6 and 7 therefore clearly illustrates that the surface area of anode electrode hardly affects the electrical characteristics of the onboard-surface Hall-type MHD generator if the distance between the anode and the cathode electrodes is the same.

Figure 8 depicts the wall heat flux for each electrode configuration case under the following two load voltage conditions: one is the optimum load voltage for each electrode configuration and the other is the load voltage with the electrical power of about 1 MW for each electrode configuration case. In addition, distributions of the wall heat flux with and without the applied magnetic field for the no-electrode case are also presented in Fig. 8. There is a considerable difference in the wall heat flux between case 1 and case 2, although the electric characteristics in case 1 and case 2 are almost the same. In case 1, the wall heat flux at the stagnation point cannot be mitigated by the MHD interaction for the load voltage with the electrical power of about 1 MW. In case 2, on the other hand, the mitigation effect of the wall heat flux at the stagnation point by the applied magnetic field can be obviously observed for the load voltage with the electrical power of about 1 MW.

Under the optimum load voltage condition, the wall heat flux at the stagnation point is slightly mitigated by the applied magnetic field even in case 1; however, the mitigation amount in case 1 is much smaller than that in case 2. As described above, case 1 and case 2 have almost the same electrical characteristics. From the viewpoint of the mitigation of the wall heat flux at the stagnation point, however, case 2 with the anode electrode placed away from the stagnation point is much better than case 1 with the anode electrode placed to cover a wide wall surface including the stagnation point.

We can find from the comparison of the distributions of wall heat flux for case 2 to case 4 in Fig. 8 that the wall heat flux at the stagnation point becomes smaller as the anode electrode is placed farther from the stagnation point. It should be also noted that the wall heat flux between the anode and the cathode electrodes decreases with increasing the load voltage for any electrode configuration. However, the wall heat flux between the stagnation point and the anode electrode has only a weak dependence on the load voltage for any electrode configuration. In case 4, the wall heat flux at the stagnation point for any load voltage is about 83% of the one without the applied magnetic field, and also the mitigation amount is almost the same as the one for the no-electrode case.

Table 1 summarizes the electrical power P, the wall heat flux at the stagnation point q_{stag}, and the total aerodynamic heating Q under the optimum load voltage condition for each electrode configuration case. The total aerodynamic heating Q is defined as

$$Q = \int_{S_{\mathrm{wall}}} q_{\mathrm{wall}}\, \mathrm{d}S \tag{20}$$

where q_{wall} is the wall heat flux and S_{wall} is the area of wall surface. It should be noted that the values of q_{stag} and Q in Table 1 are

Table 1 Electrical power P, wall heat flux at stagnation point q_{stag}, and total aerodynamic heating Q under optimum load voltage condition for each electrode configuration case

	Case 1	Case 2	Case 3	Case 4
P, MW	2.86	2.77	1.98	1.35
$q_{\mathrm{stag}}/q_{\mathrm{stag},B=0\ \mathrm{T}}$	0.94	0.87	0.84	0.83
$Q/Q_{B=0\ \mathrm{T}}$	0.85	0.81	0.74	0.72

normalized by those values without the applied magnetic field. From the comparison of the total aerodynamic heating for case 2 to case 4, we can confirm that the total aerodynamic heating becomes smaller as the anode electrode is placed farther from the stagnation point. This is because the region in which the wall heat flux can be mitigated by the MHD interaction becomes wider around the stagnation point with a peak wall heat flux.

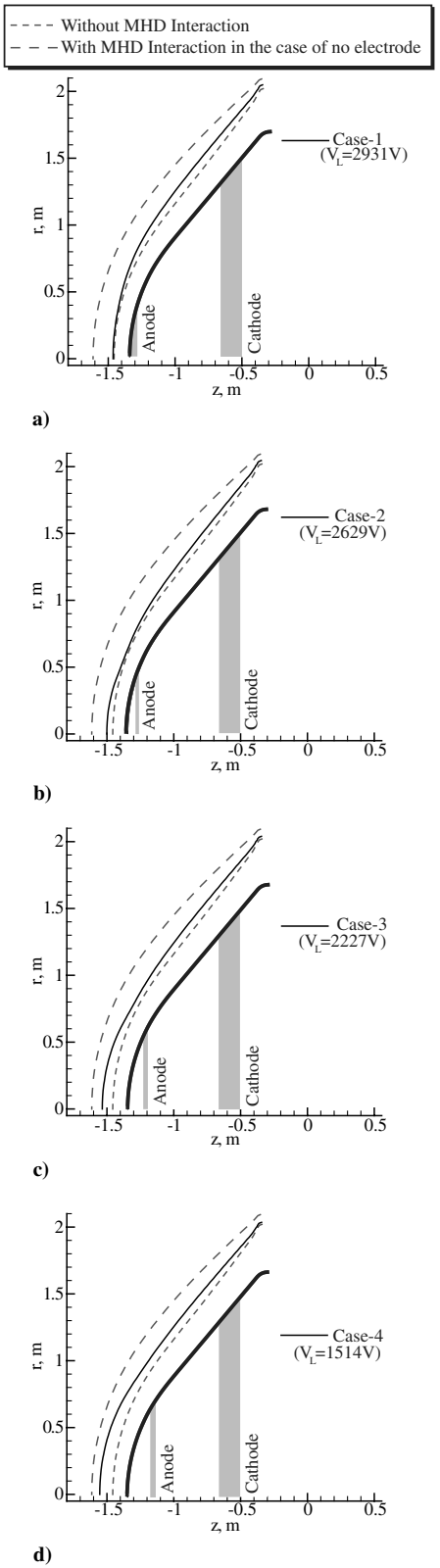

Fig. 9 Position of shock wave under optimum load voltage condition for each electrode configuration case.

Figure 9 depicts the position of shock wave under the optimum load voltage condition for each electrode configuration case. The positions of shock wave with and without the applied magnetic field for the no-electrode case are also depicted in Fig. 9. For case 1 in which the bowl-shaped anode electrode cover a wide wall surface including the stagnation point, the increase in shock standoff distance by the MHD interaction cannot be clearly observed in the region ahead of the anode electrode. This result suggests the wall heat flux around the stagnation point cannot be reduced by the MHD interaction for case 1, as shown in Fig. 8. Even for case 1, the shock standoff distance in the region ahead of the wall surface between the anode and the cathode electrodes is increased by the MHD interaction under the optimum load voltage condition. As a result, the wall heat flux between the anode and the cathode electrodes can be reduced by the applied magnetic field under the optimum load voltage condition, as shown in Fig. 8.

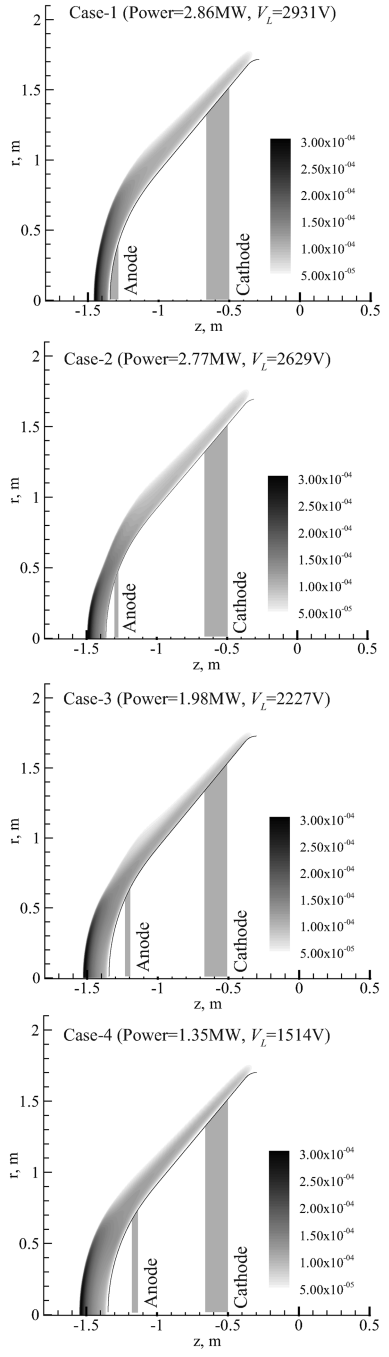

Fig. 10 Ionization degree under optimum load voltage condition for each electrode configuration case.

For case 2, case 3, and case 4 in which the ring-shaped anode electrode is placed away from the stagnation point, the increase in shock standoff distance by the MHD interaction can be observed in the region around the stagnation point as well as in the region ahead of the wall surface between the anode and the cathode electrodes, as can be found from Fig. 9. For these cases, the wall heat flux at the stagnation point as well as the wall heat flux between the electrodes can therefore be effectively mitigated by the MHD interaction unlike case 1, as illustrated in Fig. 8. We can find from the comparison of the shock standoff distance for case 2 to case 4 in Fig. 9 that the shock standoff distance in the region near the stagnation line becomes larger as the ring-shaped anode electrode is placed farther from the stagnation point.

The authors have confirmed from the computational results under various load voltage conditions that the shock standoff distance in the region ahead of the wall surface between the electrodes becomes larger with increasing load voltage for any electrode configuration. However, the shock standoff distance in the region ahead of the wall surface between the stagnation point and the anode electrode depends little on load voltage for any electrode configuration. Consequently, the wall heat flux between the electrodes decreases with increasing load voltage; on the other hand, the wall heat flux between the stagnation point and the anode electrode hardly varies when load voltage is changed, as shown in Fig. 8.

Figures 10 and 11 depict the distributions of ionization degree and electrical conductivity under the optimum load voltage condition for each electrode configuration case. For any electrode configuration, the maximum values of ionization degree and electrical conductivity are about 3×10^{-4} and 110 S/m, respectively. The authors have confirmed from the numerical results under various load voltage conditions that the plasma properties such as ionization degree, electrical conductivity, and Hall parameter in the shock layer depend

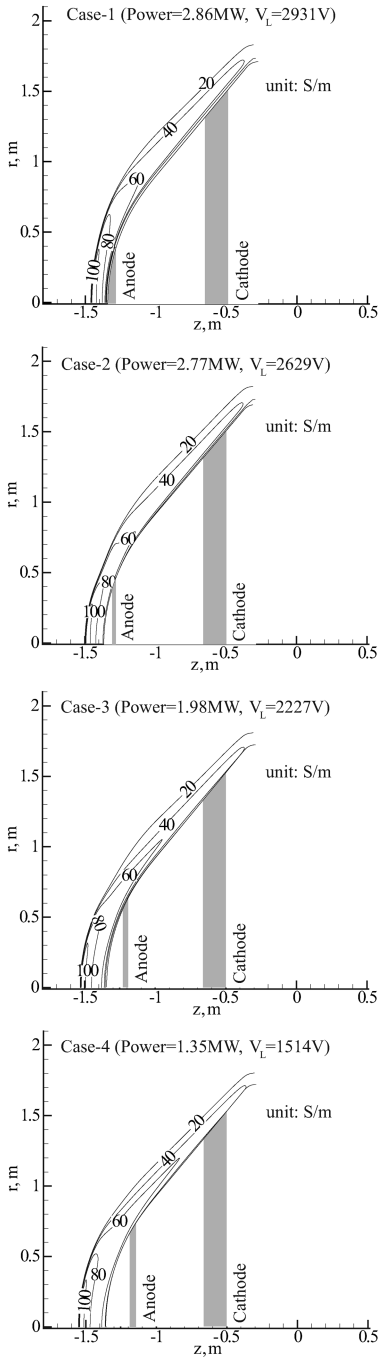

Fig. 11 Electrical conductivity under optimum load voltage condition for each electrode configuration case.

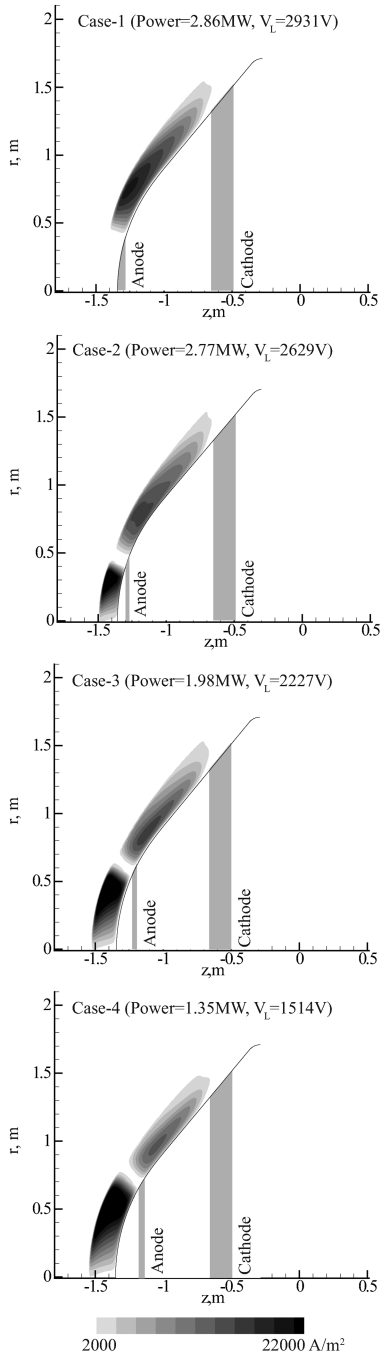

Fig. 12 Azimuthal component of electric current density under optimum load voltage condition for each electrode configuration case.

little on the load voltage for any anode electrode configuration. The value of Hall parameter in the shock layer is about 10 to 15 for any electrode configuration and any load voltage.

Figures 12 and 13 illustrate distributions of azimuthal electric current density and electric potential, respectively, under the optimum load voltage condition for each electrode configuration case. The interaction between the azimuthal electric current density and the magnetic field decelerates the plasma flow in the shock layer, leading to an increase in shock standoff distance and a decrease in wall heat flux. When the electrodynamics in the shock layer is dominated by the Hall effect, the stronger the Hall electric field induced on the *r*-*z* plane is, the larger the magnitude of the azimuthal electric current density becomes.

As can be found from Figs. 12 and 13, the Hall electric field in the region ahead of the anode electrode takes the value of almost zero for any electrode configuration. As a result, the magnitude of azimuthal electrical current density becomes considerably smaller in the region ahead of the anode electrode for any electrode configuration.

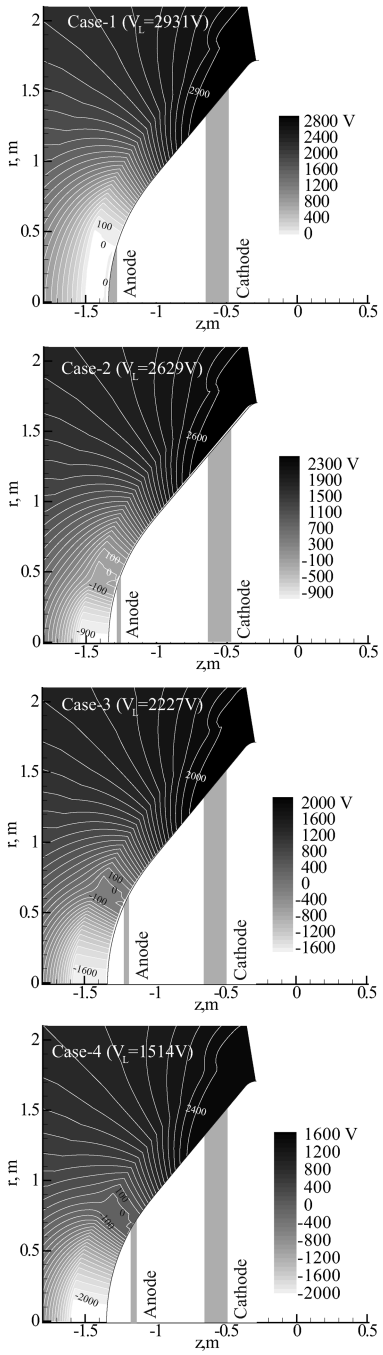

Fig. 13 Electric potential under optimum load voltage condition for each electrode configuration case.

In case 1, the strong Hall electric field cannot be induced in a wide region around the stagnation point, as shown in Fig. 13. This is because the bowl-shaped anode electrode covers the relatively large wall surface area, including the stagnation point. As a result, an MHD interaction strong enough to increase the shock standoff distance cannot be induced in the region around the stagnation point. Therefore, an effective mitigation of the wall heat flux at the stagnation point by the MHD interaction is not observed in case 1, as shown in Fig. 8. By contrast, the strong Hall electric field and the large azimuthal electric current density can be induced in a wide region around the stagnation point in case 2, case 3, and case 4, as can be found from Figs. 12 and 13. In these cases, the shock standoff distance around the stagnation line can therefore be increased and the wall heat flux at the stagnation point can be mitigated by the MHD interaction, as illustrated in Figs. 8 and 9.

The electrical characteristics in the region between the stagnation point and the anode electrode in case 2, case 3, and case 4 correspond to the electrically open-circuit condition in the theory of Hall MHD power generators (for example, [25]). The open-circuit condition induces a strong Hall electric field on the *r*-*z* plane. As a result, a large azimuthal electric current density can be obtained in the region between the stagnation point and the anode electrode in case 2, case 3, and case 4. The region with the electrical characteristics corresponding to the open-circuit condition spreads in a wider region around the stagnation point as the ring-shaped anode electrode is placed further from the stagnation point. Consequently, the mitigation effect of the wall heat flux around the stagnation point by the MHD interaction is most clearly observed in case 4, as shown in Fig. 8. The Hall electric field in the region ahead of the wall surface between the stagnation point and the anode electrode, in which the electrically open-circuit condition is satisfied, depends little on the load voltage between the anode and the cathode electrodes for any electrode configuration. As a result, as shown in Fig. 8, the wall heat flux between the stagnation point and the anode electrode is only weakly dependent on the load voltage for any electrode configuration.

On the other hand, an increase in load voltage leads to a strengthening of the Hall electric field in the region between the anode and the cathode electrodes. As a result, the MHD interaction between the anode and the cathode electrodes becomes stronger with increasing load voltage for any electrode configuration. The wall heat flux between the anode and the cathode electrodes therefore decreases with increasing load voltage for any electrode configuration, as depicted in Fig. 8.

The effects of the MHD interaction on the shock wave and the wall heat flux are more clearly observed in the no-electrode case than the other cases with the anode and the cathode electrode, as shown in Figs. 8 and 9. This is because the electrically open-circuit condition is satisfied throughout the shock layer in the no-electrode case.

IV. Conclusions

The present study has examined the aerodynamic heating and the generator performance of the reentry body equipped with the onboard-surface Hall-type MHD power generator for some different anode electrode configuration cases by means of two-dimensional numerical simulation. We have assumed that the reentry body, with a nose-radius of 1.35 m, has a pair of electrodes on the nose cone surface to function as an onboard-surface Hall-type MHD power generator. A bowl-shaped or ring-shaped anode electrode is located near the stagnation point and a ring-shaped cathode electrode is placed near the shoulder. The numerical simulation has been carried out under a flight condition with an altitude of 59.6 km and a velocity of 5.6 km/s. The strength of the externally applied dipole magnetic field supposed in the present study has been about 0.5 T. The main results in the present study can be summarized as follows.

1) The onboard-surface Hall-type MHD power generator can effectively mitigate the wall heat flux at the stagnation point as well as extract the electrical power exceeding 1 MW when the ring-shaped

anode electrode is placed on the wall surface away from the stagnation point. On the other hand, if the bowl-shaped anode electrode is placed to cover a wide wall surface including the stagnation point, an effective mitigation of the wall heat flux at the stagnation point by the MHD interaction becomes impossible, although the electrical power exceeding 1 MW can be obtained. This is because a Hall electric field strong enough to induce the strong MHD interaction cannot be obtained near the stagnation point, due to the electrically coupled circuit between the plasma and the bowl-shaped anode electrode.

2) The maximum electrical power becomes smaller as the ring-shaped anode electrode is placed farther from the stagnation point, because the distance between the ring-shaped anode and the ring-shaped cathode electrodes becomes shorter and, as a result, the power-generation volume becomes smaller. On the other hand, the mitigation amount of the wall heat flux at the stagnation point increases as the ring-shaped anode electrode is placed farther from the stagnation point. This is because the strong Hall electric field, which generates the strong MHD interaction, can be obtained in a wider region around the stagnation point when the anode electrode is placed farther from the stagnation point.

3) The wall heat flux between the ring-shaped anode and the ring-shaped cathode electrodes decreases with increasing load voltage. This occurs because the Hall electric field ahead of the wall surface between the electrodes becomes stronger with increasing load voltage. By contrast, the wall heat flux between the stagnation point and the ring-shaped anode electrode depends little on load voltage. This is because the electrically open-circuit condition is satisfied in the region between the stagnation point and the ring-shaped anode electrode, regardless of the value of load voltage between the electrodes.

The present numerical simulation has been conducted under only one flight condition. We can easily predict that the generator performance of the onboard-surface Hall-typed MHD power generator strongly depends on flight conditions, because the plasma parameters such as electrical conductivity and Hall parameter strongly depend on flight conditions. Influences of flight conditions on the generator performance will therefore be examined in our near-future study.

Acknowledgments

This study was partly supported by University of Tsukuba Research Project. A part of computation in the present study was performed with the KDK system of Research Institute for Sustainable Humanosphere (RISH) at Kyoto University.

References

[1] Meyer, R. C., "On Reducing Aerodynamic Heat-Transfer Rates by Magnetohydrodynamic Techniques," *Journal of the Aero/Space Sciences*, Vol. 25, No. 9, 1958, pp. 561–566, 572.

[2] Bush, W. B., "Magnetohydrodynamic-Hypersonic Flow Past a Blunt Body," *Journal of the Aero/Space Sciences*, Vol. 25, No. 11, 1958, pp. 685–690, 728.

[3] Ziemer, R. W., "Experimental Investigation in Magneto-Aerodynamics," *ARS Journal*, Vol. 29, No. 19, 1959, pp. 642–647.

[4] Bityurin, V. A., Zeigarnik, V. A., and Kuranov, A. L., "On a Perspective of MHD Technology in Aerospace Applications," AIAA Paper 1996-2355, June 1996.

[5] Macheret, S. O., Shneider, M. N., and Candler, G. V., "Modeling of MHD Power Generation on Board Reentry Vehicles," AIAA Paper 2004-1024, Jan. 2004.

[6] Wan, T., Gandler, G. V., Macheret, S. O., Shneider, M. N., and Miles, R. B., "CFD Modeling and Simulations of MHD Power Generation During Re-Entry," AIAA Paper 2004-2562, June 2004.

[7] Wan, T., Suzuki, R., Gandler, G. V., Macheret, S. O., and Shneider, M. N., "Three Dimensional Simulation of Electric Field and MHD Power Generation During Re-Entry," AIAA Paper 2005-5045, June 2005.

[8] Fujino, T., and Ishikawa, M., "Numerical Simulation of Control of Plasma Flow with Magnetic Field for Thermal Protection in Earth Reentry Flight," *IEEE Transactions on Plasma Science*, Vol. 34, No. 2, 2006, pp. 409–420.
doi:10.1109/TPS.2006.872458

[9] Fujino, T., Funaki, I., Sugita, H., Mizuno, M., and Ishikawa, M., "Influences of Electrical Conductivity of Wall on Magnetohydrodynamic Control of Aerodynamic Heating," *Journal of Spacecraft and Rockets*, Vol. 43, No. 1, 2006, pp. 63–70.
doi:10.2514/1.13770

[10] Fujino, T., and Ishikawa, M., "Numerical Studies of Magnetohydrodynamic Flow Control Considering Real Wall Electrical Conductivity," *Journal of Spacecraft and Rockets*, Vol. 44, No. 3, 2007, pp. 625–632.
doi:10.2514/1.25824

[11] Fujino, T., Yoshino, T., and Ishikawa, M., "Numerical Analysis of Reentry Trajectory Coupled with MHD Flow Control," *Journal of Spacecraft and Rockets*, Vol. 45, No. 5, 2008, pp. 911–920.
doi:10.2514/1.33385

[12] Yamamoto, Y., "Recent Comparisons of Aerothermodynamic Results by CFD and FEM Coupling Analysis with OREX Flight Experiments," *Proceedings of the 13th NAL Symposium on Aircraft Computational Aerodynamics*, National Aerospace Lab. of Japan, Tokyo, 1995, pp. 27–39.

[13] Fujino, T., and Ishikawa, M., "Feasibility of an On-board Surface Hall MHD Power Generator in Reentry Flight," *Journal of Propulsion and Power*, Vol. 25, No. 1, 2009, pp. 83–93.
doi:10.2514/1.33354

[14] Kang, S. W., Jones, W. L., and Dunn, M. G., "Theoretical and Measured Electron-Density Distributions at High Altitudes," *AIAA Journal*, Vol. 11, No. 2, 1973, pp. 141–149.
doi:10.2514/3.50446

[15] Park, C., "Assessment of Two-Temperature Kinetic Model for Ionizing Air," *Journal of Thermophysics and Heat Transfer*, Vol. 3, No. 3, 1989, pp. 233–244.
doi:10.2514/3.28771

[16] Gnoffo, P. A., Gupta, R. N., and Shinn, J. L., "Conservation Equations and Physical Models for Hypersonic Air Flows in Thermal and Chemical Nonequilibrium," NASA TP-2867, Feb. 1989.

[17] Millikan, R. C., and White, D. R., "Systematics of Vibrational Relaxation," *Journal of Chemical Physics*, Vol. 39, 1963, pp. 3209–3213.
doi:10.1063/1.1734182

[18] Mitchner, M., and Kruger, C. H., *Partially Ionized Gases*, Wiley, New York, 1973, Chap. 2.

[19] Sutton, G. W., and Sherman, A., *Engineering Magnetohydrodynamics*, Dover, New York, 2006, Chap. 5.

[20] Gupta, R. N., Yos, J. M., Thompson, R. A., and Lee, K. P., "A Review of Reaction Rates and Thermodynamic and Transport Properties for an 11-Species Air Model for Chemical and Thermal Nonequilibrium Calculations to 30,000 K," NASA RP-1232, Aug. 1990.

[21] Rosa, J. R., *Magnetohydrodynamic Energy Conversion*, McGraw–Hill, New York, 1968, Chap. 2.

[22] Wada, Y., and Liou. M-S., "A Flux-Splitting Scheme with High-Resolution and Robustness for Discontinuities," AIAA Paper 94-0083, Jan. 1994.

[23] Yamamoto, S., "Shock-Vortex Capturing Method and Its Application to Unsteady 3-D Cascade Flow," *Computational Fluid Dynamics Journal*, Vol. 8, No. 2, 1999, pp. 341–349.

[24] Yoon, S., and Jameson, A., "Lower-Upper Symmetric-Gauss-Seidel Method for the Euler and Navier-Stokes Equations," *AIAA Journal*, Vol. 26, No. 9, 1988, pp. 1025–1026.
doi:10.2514/3.10007

[25] Eberhardt, S., and Imlay, S., "Diagonal Implicit Scheme for Computing Flows with Finite Rate Chemistry," *AIAA Journal*, Vol. 6, No. 2, 1992, pp. 208–215.

[26] Fujino, T., Funaki, I., Sugita, H., Mizuno, M., and Ishikawa, M., "Numerical Analyses on Flow Control around Blunt Body 'OREX' by Magnetic Field," AIAA Paper 2003-3760, June 2003.

[27] Lobb, R. K., "Experimental Measurement of Shock Detachment Distance on Spheres Fired in Air at Hypervelocities," *The High Temperature Aspects of Hypersonic Flow*, edited by W. C. Nelson, Pergamon, New York, 1964, pp. 519–527.

[28] Yuhara, M., Fujino, T., and Ishikawa, M., "Numerical Analysis of Effects of Liquid Particles on Plasmadynamics in a Large-Scale Pulsed MHD Generator," AIAA Paper 2004-2369, June 2004.

[29] Mizukoshi, R., Matsumoto, Y., Fujino, T., and Ishikawa, M. "Design and Performance Analysis of Large Scale Nonequilibrium Disk MHD Generator," AIAA Paper 2007-4241, June 2007.

J. Blandino
Associate Editor